Synthesis of Carbon–Metal Multi-Strand Nanocomposites by Discharges in Heptane Between Two Metallic Electrodes

A. Hamdan, H. Kabbara, M.-A. Courty, M. Cha, J.-M Martinez, T. Belmonte

SYNTHESIS OF CARBON-METAL MULTI-STRAND NANOCOMPOSITES BY DISCHARGES IN HEPTANE BETWEEN TWO METALLIC ELECTRODES

A. Hamdan[1], H. Kabbara[2], M.-A. Courty[3], M. S. Cha[1], J.-M. Martinez[5], T. Belmonte[2,4*]

[1]King Abdullah University of Science and Technology, (KAUST), Clean Combustion Research Center (CCRC), Thuwal 23955–6900, Saudi Arabia.

[2]Université de Lorraine, Institut Jean Lamour, UMR CNRS 7198, NANCY, F-54042, France.

[3]UPR 8521 PROMES CNRS. Procédés et Matériaux Solaires. Tecnosud. 66100 Perpignan, France.

[4]CNRS, Institut Jean Lamour, UMR CNRS 7198, NANCY, F-54042, France

[5]UPR 8521 PROMES CNRS – Univ. Perpignan. Tecnosud. 66100 Perpignan, France.

* corresponding author. Email: thierry.belmonte@univ-lorraine.fr

PACS number: 81.16.Dn Self-assembly; 81.05.Lg Polymers and plastics; rubber; synthetic and natural fibers; organometallic and organic materials; 52.80.Wq Discharge in liquids and solids.

Keywords: discharge in liquids; nanoparticle synthesis; metal/carbon nanocomposite, dielectrophoresis.

ABSTRACT

We studied composite wires assembled from electric field-driven nanoparticles in a dielectric liquid (heptane) to elucidate the exact processes and controlling factors involved in the synthesis of the multi-phase nanocomposites. Filamentary wires are synthesized by a two-step process: (1) abundant nanoparticle production, mostly of carbonaceous types, from heptane decomposition by spark discharge and of metal nanoparticles by electrode erosion and (2) assembly of hydrogenated amorphous carbonaceous nano-clusters with incorporated metal nanoparticles forming wires by dielectrophoretic transport while maintaining a high electric field between electrodes kept sufficiently separated to avoid breakdown. Four types of nanocomposites products are identified to form at different steps in distinctive zones of the setup. The black carbonaceous agglomerates with metal spherules made by electrode erosion represent the pyrolytic residues of heptane decomposition by spark discharge during step 1. The filamentary wires grown in the interelectrode gap during step 2 get assembled by dielectrophoretic transport and chaining forces. Their great stability is shown to express the concurrent effect of polymerization favoured by the abundance of metal catalysts. The nature, abundance, and transformation of solid particles from the source materials versus discharge conditions control the morphological and compositional diversity of the wires. The production of mineral and metal nano-particles traces the efficiency of dielectrophoresis to separate compound particle mixtures by size and to co-synthesize nanostructured microcrystals and nanocomposites.

The link between impurities and the variability from nano- to micro-scales of the synthesized products provides an innovative contribution to the knowledge of nanocomposite synthesis triggered by electric field.

1. INTRODUCTION

Research conducted on nanoparticles and nanocomposites synthesized by discharges in liquids have devoted considerable attention to elucidate the involved processes and the factors controlling the properties of the final products depending upon the precursor materials and the experimental setup. Electrode erosion and/or liquid conversion have been shown to produce nanoparticles at high rate by discharges in liquids [1–5]. They can also be used to grow other nanostructures like nanowires, mostly by the Vapor-Liquid-Solid mechanism [6–8]. Yao *et al.* [9] have proposed to view the synthesis by discharges in liquids of uniform CuO nanorods with sharp ends from tiny nanoparticles as a three-step process: (1) rapid oxidation of Cu nanoclusters, (2) spontaneous aggregation of CuO nanoparticles, and (3) Ostwald ripening. A similar synthesis of one-dimensional CuO nanocrystals using the pulsed wire explosion technique in deionized water was documented by Krishnan *et al.* [10] but rather explained as a selective formation of spherical Cu nanoparticles or one-dimensional CuO nanocrystals due to modulation of the exploding medium temperature. The oriented spindly nanocrystals would trace the effects of Brownian coagulation which starts at about 35°C in the conditions of Krishnan's work in the continuation of Ostwald ripening, which prevails at low temperature.

Xie *et al.* [11] varied the concentration of cetyltrimethylammonium bromide (CTAB) in an ascorbic acid solution to regulate the organization shapes of Cu nanoparticles. The rod-like micellar template of the CTAB would be favorable for synthesizing one-dimensional nanomaterials.

Hermanson *et al.* [12] revealed the great potential of dielectrophoresis to form microwire assembly of metallic nanoparticles from aqueous colloidal suspension, or even of complex structures, in mixed suspensions of metallic and polystyrene particles. This technology refers to the mobility and interactions of nanoparticles, whether they are charged or not, when subjected to a non-uniform electric field. The growth of the wires starts above a threshold

defined by the field strength and occurs in the gap between planar electrodes at a speed faster than 50 micrometers per second. Hermanson *et al.* [12] reported the effect of larger particles on the stronger interparticle attractions, thus resulting into mechanically stable wires in spite of their high porosity.

The microwire synthesis by electrical fields was explored further by Velev *et al.* [13] who recognized a two-step process. The first step is the alignment of particles by attractive dipolar interparticle interactions along the direction of the electric field lines into cylindrical or half-cylindrical structures of micrometer diameters, defined as the "chaining" force. The second step is the assembly of the microwires by the dielectrophoretic effect into complex structures, recognized to be stable even after removal of the applied electric field. In addition, Velev *et al.* [13] also documented how the combined action of dipole-field (DEP) and dipole–dipole chaining interactions could synthesize colloidal crystals showing one axis aligned along to the electric field. This electrically-triggered crystallization process was observed to be controlled by the type of particles because the denser ones suffer stronger sedimentation forces acting against the assembly by chain forces and dielectrophoresis [13]. Lumsdon *et al.* [14] pointed how the DEP-driven assembly efficiently separates compound particle mixtures by size, thus resulting into the co-synthesis of distinctive pure crystals.

Using a rather different experimental setup, Hamdan *et al.* [15] also reported a two-step synthesis of nanoparticle assembly of micro-wires from a dielectric liquid under high electric field. First, the discharges between electrodes at 100 µm gap distance decompose a liquid hydrocarbon (*e.g.,* heptane), thus resulting in the production of nanoparticles, mostly of carbonaceous types. Then, the increased gap distance to at least 1 mm avoids electric breakdown, thus suppressing heptane decomposition. High-speed imaging technique helped to view the synthesis of composite wires formed of 2 or 3 strand assembly by DEP until the depletion of nanoparticles in the liquid was achieved [15]. Their first characterization

documented a bi-phase assemblage showing the metallic nanoparticles issued from the electrode erosion embedded within a hydrogenated amorphous carbonaceous matrix. The later was suggested to derive from agglomeration of the nanoparticles that were produced by the dielectric liquid decomposition [15]. The non-conductive property of the composite wires, which can be a few millimeters long, has shown that the percolation threshold was not reached in spite of the high concentration of metallic nanoparticles in the carbonaceous matrix. We present here further exploration of composite wires assembled from electric field-driven nanoparticles in a dielectric liquid (heptane) in order to elucidate what are the exact processes and controlling factors involved in their synthesis.

2. EXPERIMENTAL SETUP

A new run of experiments was performed using the same operational setup and the same conditions as the ones formerly established [16]. A positive high voltage is applied to one pin-electrode while the other is grounded. The effects of nanoparticle composition issued from the electrode erosion on the synthesized nanocomposites were investigated by comparing different materials of similar wire electrodes (1 mm in diameter): platinum, aluminium, nickel, copper, tungsten, and carbon. Experiments were run in two steps. The first step was operated in similar conditions (applied voltage: +10 kV, gap distance: 100 µm, and liquid medium: heptane) for about one hour of successive discharges ignited at 10 Hz. This corresponds to the production of hydrogenated amorphous carbonaceous nanoparticles (HAC) from decomposition of heptane and of metallic nanoparticles (~5% in weight) issued from the electrode erosion. About six thousand discharges were ignited to load the dielectric liquid in HAC nanoparticles. The second step consists in increasing the gap distance to 1 mm and keeping the high voltage constant at +10 kV or increased up to + 15 kV was controlled not to induce breakdown in heptane while an intense electric field (15 MV m^{-1}) was maintained in

the inter-electrode gap space. An ultrafast camera FASTCAM SA5 (model 1000K-M3) was used to observe the growth of the wire during the second step and its movement in the inter-electrode gap. Pictures were acquired at rate of 250 images-per-second for a corresponding window of 256×128 pixels. Composite products (*i.e.,* filamentary wires, agglomerates, crystallized minerals, and metal particles) were collected by sedimentation on a silicon wafer, located under the pin-electrodes, which was retrieved after total evaporation of the heptane.

The various composites were at first directly observed from the silicon wafer using a Scanning Electron Microscope (SEM), FEI XL 30 equipped with micro-EDX (Energy-Dispersive X-ray) and TLD detector (Through the Lens Detector) for chemical analysis and high-resolution imaging, respectively. A selection of the synthesized products was then displayed on a carbon tape for performing high-resolution SEM characterization at stable conditions. The structure at high-resolution of the composites together with their chemical composition and crystallinity was studied using a Transmission Electron Microscope (Philips CM200). A Fourier Transform Infra-Red (FTIR) spectrometer, Cary 600-Agilent Technology, was used to identify chemical bonds in by-products. This study focuses on the comparison of the composition and structure of the composite by-products that were deposited on the electrodes and on the silicon wafer after the step 1 and step 2 operations.

3. RESULTS AND DISCUSSION

3.1. Visual control of the multi-strand wire growth

As we formerly described [16], the control with the ultrafast camera allows the following of the two-step process that leads to the formation of multi-strand wires in these operational conditions (**figure 1)**.

The first step consists of about six thousand discharges that are ignited to load the dielectric liquid in HAC nanoparticles from the heptane decomposition and to a minor extent (~5% in weight) in metallic nanoparticles due to the electrode erosion. Then, electrodes are moved far enough from each other to grow wires by dielectrophoresis from suspensions of nanoparticles. No breakdown is then possible under these conditions. In fact, the wire could be observed only once its diameter became thick enough, so that the structure could be visible on camera records. In **figure 2**, the time evolution of material formation within the inter-electrode gap area, where a wire is moving, is depicted. At the beginning, the inter-electrode gap is free of wires. After 40 ms only, a dark thread becomes clearly visible near the center of electrodes axis and crosses the gap, connecting to both electrodes. This resulted in the formation of wires of about 1 mm in length in less than 40 ms. This gives a growth rate of ~25,000 µm s^{-1}, to be compared with the growth rate (> 50 µm s^{-1}) mentioned by Hermanson *et al.* [12]. This change in the growth rate of wires might be attributed to differences in nanoparticle size (5-10 nm here [15] *vs* 15-30 nm in [12]), applied voltage (10,000 V *vs* 50-250 V) and inter-electrode gap distance (1 mm *vs* 2-10 mm). The main feature of this primary wire, whose movement is presented in **figure 2**, is that it is already as long as the gap distance on the initial period of time. Then, as time passes, it becomes thicker. At 1.63 s, a second wire is clearly observed and likely appears from 1.50 s on when a dot shows up (see circle in **figure 2**) on left-hand side of the gap, which acts as an inception point for the second wire. Then, wires are entangled and likely spin around the electrode axis, such that they are successively nearer or farther from the electrode axis. At 4.912 s, a new discharge occurs. Although the gap discharge is too large to have breakdown in heptane, as explained before, the enrichment of the liquid by nanoparticles allows breakdown after a sufficient large number of discharges. Then, we observe fragments in the liquid and a new wire bridging the gap 12 ms later. This

new wire was not formed during this time lapse but formerly, so that it got trapped between the electrodes.

In our experiments, observing an already-synthesized wire in the inter-electrode gap is subjected to several conditions. First, the liquid must be submitted to convection to bring the wire in the vicinity of the gap. The fluid velocity must not be too high anyway, otherwise the wire cannot be trapped between the electrodes. This depends also on the applied voltage. Indeed, the wire is submitted to the following forces: buoyancy, the electrostatic force due to the applied voltage, and convection induced by the fluid motion after discharges. Practically, several attempts are needed to meet the proper conditions and capture a wire in the gap. Then, there will be no potential confusion between a wire formed in the inter-electrodes region and a wire formed elsewhere and trapped between the electrodes. To conclude, we readily understand that if the synthesis of a wire is a fast process (~25,000 $\mu m\ s^{-1}$), the formation of multi-stranded wires takes time (several seconds as shown in **figure 2**). Indeed, the presence of the electric field greatly affects the parallel and perpendicular components of the nanoparticle mobility. Transport towards the lateral surface of the wire is by far much slower than to the wire ends.

The way strands get entangled can be partly clarified by changing step by step the inter-electrode gap distance (**figure 3**). First, the electrodes are moved closer one from the other (from ~2.2 mm to 0.25 mm) and in a second step, they are moved farther (from 0.25 mm to ~1.7 mm). Every 30 seconds, the gap distance is changed and a picture is taken. When the electrodes are far one from the other, strands which are shorter than the inter-electrode gap distance are stretched by the electric field. We notice that several strands are attached to each electrode tip. When the electrodes are moved closer and closer one to the other (**figure 3a**), strands get entangled, and the longest wires fold several times and form a ball. On the other hand, when electrodes are pulled away one from the other (**figure 3b**), strands unfold and get

untangled. This reversible behaviour indicates that strands do not bind together in these conditions and that another assembling process must be at stake to assemble several strands into a single wire. This shows that the binding of the strands to form a multi-strand wire is not mechanical, but would more likely require a cementing agent, the nature of which is discussed in the following section.

Another important aspect shown by this image is that, because of erosion, pin electrodes no longer exhibit a sharp tip with high radius curvatures after several discharge events, but a flat tip (**figure 3**). The patterns of the electric field lines are affected by this change, and several parallel strands get stacked vertically as it is visible on the topmost image in **figure 3a**. Consequently, assembling strands into a 2D ribbon becomes more likely than forming a cylindrical wire, as mentioned earlier.

3.2. Structure and composition of the synthesized nanocomposites

The by-products that were deposited on the electrodes and on the silicon wafer after the step 1 and step 2 operations can be separated into four types of composites based on their composition and morphology at various scales, all showing nanostructured patterns at nanoscales. These products, now defined as nanocomposites, comprise (**figures 4 and 5**): (1) black carbonaceous agglomerates, (2) translucent to coloured carbonaceous filamentary wires, (3) metal particles, and (4) mineral particles. The visual control with the ultrafast camera has helped us to estimate where and at what exact stage of the discharge process made the different synthesized nanocomposites (**table 1**).

Type 1. The black carbonaceous agglomerates

The type 1 agglomerates have been collected on the wafer and on the anode after the step 1 and step 2 operations (**figure 5**). They are abundant as scattered heaps on the wafer when

using the aluminium electrodes and form a nearly continuous deposit when using the copper electrodes. They are rare to exceptional for the carbon, platinum, and tungsten electrodes. They displayed fine cracks and elongated vesicles, and they are strongly stick to the silicon wafer. The absence of fine cracks in the agglomerates occurring on the anode helped us to interpret that they formed on the anode due to decomposition of heptane by the step 1 spark discharge, whereas they were deposited on the wafer during the final evaporation from the carbon black that formed by spark discharge decomposition of heptane mostly during step 1 operation.

They contain numerous poorly sorted metal spherules (nano to micron-sized) identical in composition to the involved electrodes. This characteristic is useful to trace the sensitivity of the electrode to the erosion initiated by the step 1 discharge. The spherules are formed of densely packed platy metal flakes ranging in size from 50 to 200 nm. The cracked agglomerates displayed a homogeneous, dark brown to black fine mass, with abundant micron-sized vesicles, which consist of poorly crystallized graphitic carbon based on FTIR analysis. At higher magnification, the fine masse consists of randomly packed nano-sized particles that are locally forming short (< 100 µm) filamentary nanostructures. In addition to the spherules from the electrodes, a few angular, micron-sized, nanostructured inclusions made of barium sulphate and rare-earth oxides occur within the fine mass. The same inclusions are also present in type 1 agglomerates of the aluminium anode in which they locally form dense concentrations.

Type 2. The filamentary wires

The filamentary wires have been encountered only after step 2 operation and collected on the wafer after evaporation of heptane. In order to avoid mixing of the different products, only the

ones deposited in wafer zones free of the type 1 agglomerates have been taken into consideration and selectively sampled for high-resolution characterization.

Based on marked contrast in morphology of the filamentary wires and composition of their matrix with associated inclusions, four sub-types of filamentary wires have been identified to occur together after each experiment. They comprise (**figures 4 & 6, table 2**): (a) cylindrical, single micron-sized filamentary wires of diverse colours (blue, red, translucent or black) that are several millimeters long and composed of densely packed, twisted nano-sized filaments, (b) translucent to white, micron-sized, multi-filament wires of several millimeters long, often in the form of imbricated bundles with a twisted morphology, (c) flat translucent films showing a crumpled paper-like pattern without distinctive long wires, and (d) flat white to pale yellow multi-filament wires often showing distinctive microstructures of plant tissues. The four sub-types were encountered together for the experiments performed using the aluminum electrodes; the sub-type (a) was dominant for the copper electrodes, only a few of sub-types (c) and (d) were observed for the carbon, platinum, and nickel electrodes.

Based on the visual control using the ultrafast camera, the type 2 nanocomposites are assumed to correspond to the filamentary wires that were observed growing in the inter-electrode gap during the step 2 operation. The few filamentary wires collected on the silicon wafer, when compared with the great number of wires that appear to have formed during the 20 mn experiment, suggest that part of them were either lost during the evaporation procedure or not preserved as solid products in the heptane before its total evaporation. The good resistance of the remaining ones to the manipulation, or under the electron beam when performing high-resolution characterization, attests for their remarkable structural stability under high-energy exposure. The four sub-types of filamentary wires contain abundant inclusions of two types (**figure 7**): (i) nano- to micron-sized nanostructured spherules showing a composition identical to the one of the electrodes and (ii) angular to filamentary micron-sized inclusions

showing a highly variable composition that consists of oxides, sulphates and sulphides, carbonates and carbide, and pure or alloy metal components (**table 2**) which are also nanostructured; often the inclusions formed of calcium carbonate with distinctive faces and angular edges have clearly the typical morphology of nanostructured micro-crystallites. The inclusions can be either isolated particles or clusters of heterogeneous composition. They can be embedded within the carbonaceous matrix or weakly attached to the wire wall, particularly for the metal ones. Often the latter, when manipulated for sample preparation, detached from the filamentary wire. The limited number of filamentary wires collected has not allowed the establishment of a solid correlation between the compositional range of the micron-sized inclusions and the type of filamentary wires. The similar sub-types of filamentary wires produced with the different sets of electrodes (Al, Pt, Cu, and Ni) mostly differ by the composition and abundance of nano- to micron-sized spherules that are inclusions from the eroded electrodes and incorporated into the carbonaceous matrix during the growth process.

Observation at high resolution (**figure 8**) shows marked contrast of the nanostructural pattern between the different sub-types of filamentary wires, between the ones from a same sub-type and even between different parts of the same wire, particularly for sub-type 2b, 2c, and 2d. The finest mode of nanostructuration is an assembly of elementary nanoparticles that range in size from a few nm to 50-100 nm. They can be densely assembled in twisted nanostructured films (**figure 8a**), densely imbricated and regularly aligned forming elementary nano-sized filaments (**figure 8b**), irregularly imbricated with no preferential alignment (**figure 8c**), or present as porous agglomerates that are organized only locally as micron-sized filaments. The sub-type 2c (crumpled like-paper films) shows a marked contrast between a finely folded, homogeneous, carbonaceous matrix exhibiting no structure and agglomerates made of nanostructured, micron-sized filaments (**figures 9a & 9b**). At high resolution, the cell structure of the tissue-like sub-type 2d appears very well preserved and the elementary

filaments revealed to be formed of twisted plant fragments (**figure 8d**). Calcium carbonate micro-crystallites have been identified only for the sub-type 2d in which they appear often as regularly-spaced particles that are associated to cell structures (**figures 9c & 9d**).

At high-resolution SEM (**figure 10a**), mineral and metal nanoparticles of the same size range are also identified as scattered within the hydrocarbon matrix. However these components are more easily characterized when occurring as distinctive micron-sized grains that are in most cases formed of densely-packed coarse nanoparticles (100-500 nm). The TEM observation (**figures 10b and 10c**) gives a better view of the dense network of metal and mineral nanoparticles, which are both issued from the electrode erosion and from the heptane impurities within the HAC matrix. The TEM images clearly show that these nanoparticles most often appear in the form of a rather open chain network within the HAC matrix and never as dense agglomerates.

Locally-resolved EDX measurements (data are available on demand) show that the amount of metal and mineral in the filamentary wires never exceeds a few weight percent.

Type 3. The metal particles

In addition to the ones bounded and attached to the filamentary wires as described above, metal particles of similar composition (Ni, Cu, Fe, Cu-Zn, Cu-Ni, V-Fe-Cu-Zn for the most common) and nanostructure have been encountered on the cathode to which they are strongly attached and within cracks of the type 1 agglomerates from which they can be easily removed (*e.g.*, **figure 5c & 5d**).

Type 4. The mineral particles

In addition to the micron-sized ones that are embedded within the HAC matrix of the wire, coarser mineral particles (15 to 40 µm) have been encountered either as isolated grains or

finely incorporated into the multi-filamentary wires (**figure 11**). They can be sub-angular composite agglomerates formed of poorly-sorted micron-sized calcium carbonate, silicon oxide, and titanium oxide nanoparticles with tiny metal inclusions, which are embedded by nano-sized carbonaceous films. Angular single-phase mineral grains with sharp edges showing evidence of nanostructuration on their faces, metal inclusions in the anfractuosities, and carbonaceous domains have also been observed. Pure silica, silicon, and diverse alumino-silicate minerals have been identified.

3.3 FTIR data

Spatially-resolved FTIR measurements were performed on the filamentary wires that were produced between the different types of electrodes (Cu, Ni, Al, C, and W), (**figure 12**). The most intense absorption bands are assigned to the following contributions. Peaks at 2921 cm^{-1} and 2852 cm^{-1} are assigned to methylene C–H asymmetric and symmetric stretch vibrations, respectively. Peaks at 2954 cm^{-1} and 2867 cm^{-1} are assigned to methyl C–H asymmetric and symmetric stretch vibrations, respectively. Peaks due to methylene C–H bending and methyl C–H asymmetric bending are expected near 1470 and 1455 cm^{-1}, respectively, and overlapped to give the contribution observed at 1461 cm^{-1}, mainly in the case of C and W electrodes. Rovibrational contributions centred at 1602, 2349, and 3784 cm^{-1} are undoubtedly due to CO_2. The broad peak due to OH stretching is found around 3380 cm^{-1}. In the case of Al, Ni, and Cu electrode, skeletal vibrations due to C–C backbones in long carbonaceous chains are likely present between 1180 and 925 cm^{-1}. The presence of skeletal vibrations when Ni, Al, and Cu metallic nanoparticles are in the liquid, suggests that the decomposition of heptane is affected by these catalytic elements. Their presence would favour the synthesis of long-chain molecules. In the case of C and W, this effect is not observed because the

erosion of these materials is known to be limited due to their high melting point (3800 K for C and 3695 K for W *vs* 933 K for Al, 1728 K for Ni, and 1358 K for Cu).

3.4. Forming processes of the synthesized nanocomposites

The structure and composition of the synthesized nanocomposites collected for the successive experiments using different electrodes and the assistance of the visual control provided by the ultrafast camera now allow us to establish where, how, and from what precursor materials each type was formed.

The marked contrast in spatial distribution, composition, and structure between the type 1 black agglomerates and the type 2 filamentary wires with their specific inclusions can be interpreted to represent two distinct transformation products of the heptane to different intensities of the applied electric field. The type 1 products showing the characteristics of pyrolitic residues (*e.g.*, amorphous soot to graphitized carbon black) trace the products formed by decomposition of the heptane at first during the step 1 spark discharge and then to a minor extent by lower energy thermal decomposition of the heptane due to maintenance of the electric field during the step 2 operation. The agglomerates encrusted on the anode would be mostly issued from the step 1 spark discharge, whereas the ones on the silicon wafer integrate pyrolytic residues from the two steps. Although the mineral inclusions associated with the type 1 agglomerates have a similar composition on the anode and on the wafer, the greater abundance in the former clearly attests that step 1 high-energy electric discharge has decomposed a higher amount of heptane as compared to the step 2 phase. In addition, the occurrence of the type 3 metal particles firmly attached to the cathode illustrates the efficiency of the step 1 spark discharge to have separated components according to their respective charge: positive ones on the cathode (metals) and negative ones on the anode (carbon and salt-based volatiles). In contrast, the type 3 metal particles trapped within the

cracks of the type 1 agglomerates on the silicon wafer obviously represent the latest particles that synthesized in the liquid heptane at the end of the step 2 operation. The structural and compositional similarities of the metal-nanostructured particles between step 1 and step 2 phases show that a similar process of metal separation from impurities originally present in the precursor materials has been maintained from step 1 to step 2 in spite of the lower intensity. The evidence for the synthesis of the type 1 pyrolytic residues by high-energy electric field allows us to clearly reinforce the production of the type 2 filamentary wires by low energy electric field, *i.e.*, mostly the one exerted for 20 mn during the step 2 operation without electric discharge. Thus, their formation results from reorganization of C-H compounds during the step 2 break that was made possible due to the low-energy electric field, whereas during the previous step 1 the repeated electric discharges were continuously breaking the most fragile C-H bonds. The control of the ultrafast camera helps us to clearly visualize how the molecular fragments that were produced by the high-energy decomposition of heptane during the step 1 electric discharge accumulated in the inter-electrode domain due to maintenance of the applied electric field. Reorganization of the broken molecular fragments might have also occurred during the step 2 operation throughout the entire liquid due to their dispersion following the electric discharge. These components would most likely correspond to the nanostructured microfilaments that were identified within the fine mass of the type 1 carbonaceous agglomerates. Their specific characterization that would have required performing selective filtration of the heptane at the end of the experimentation was not the scope of our study. However, the overall production of abundant nano-sized bricks from the activated molecular fragments formed in the entire spark-affected domain is obviously the initial stage of the nanocomposite synthesis due to the electric discharge. In this direct effect of plasma-driven processes, the primary clusters would randomly reorganize by diffusion limited aggregation [16, 17], therefore showing at nano- to micro-scale a fractal-like assembly

that is not constrained by the long-applied electric field. In contrast, the dielectrophoretic particle transport obviously controls the filamentary growth of the type 2 nanocomposites which can be achieved only when liquid breakdown and plasma formation have ended, or at best in domains not affected by these two processes. The close resemblance between the nanostructural pattern particular to the termination of the subtype 2b wires obtained by the present in-liquid discharge process (**figure 13**) with the ones formerly described for wires synthesized by dielectrophoresis [12] brings solid support to explain the growth of filamentary nanocomposites by this mechanism. The visual control with the ultrafast camera does confirm how aggregation starts where nanoparticles accumulate to form the incipient stage of filamentary nanostructure which is then supplied by increased concentration of nanoparticles at the end of the wire as previously pointed by Hermanson *et al.* [12].

This observation highlights the critical role played by the tips of the nanostructured filamentary wires to sustain a continuous growth and to prevent depletion effects at the tips, illustrated as well by the granular structure at nanoscale of single strand (**figure 10a**). The overall similarity between the type 2 filamentary wires produced using different sets of electrodes (Al, Pt, Cu, and Ni) together with the minor contribution of nanoparticles eroded from the electrodes to the nanocomposite supply shows that occurrence of the latter is certainly important for the filament growth, although it might not be the leading mechanism. The occurrence of similar features for the different electrodes and the minor proportion of metal spherules issued from electrode erosion clearly show that the metal components do not form the skeleton of the filamentary wire, although their scattered presence is critical for consolidating the HAC nanoparticle-chain assembly into stable filamentary wires. In addition, the contrast between the visual control with the ultrafast camera that showed the production of many filamentary wires during the 20 mn step 2 operation and the few filamentary wires which could be collected after total evaporation of heptane implies that the latter would

represent only the most stable filamentary nanocomposites. This observation incites to consider that the dielectrophoresis process can certainly explain the chain-like assembly of nanoparticles but not the formation of the strong bonds between nanoparticles, which is required to produce solid filamentary wires. In fact, the joint occurrence of compositionally variable nanoparticles within a C-H film with no apparent structure, together with the presence of metal nanoparticles, show that the latter have acted as catalysts to allow nucleation and growth of the C-H matrix from molecular clusters by gas/liquid polymerization during step 2. The similar stability of the filamentary nanoparticle assembly synthesized with the different electrodes and the common occurrence within the C-H matrix of diverse metal and mineral nanoparticles clearly indicate that two joint processes produced nanocatalysts: the step 1 electrode erosion and the segregation of impurities from the precursor materials. This is also well corroborated by the synthesis of type 2 filamentary wires using graphite electrodes that are morphologically similar at nano- to micro-scales to the crumpled paper-like type 2c wires obtained using other metallic electrodes (**figure 14a**). The TEM images show that instead of metal nanospherules the contribution of the electrode erosion is also represented by nano-sized particles here made of pure carbon that are embedded in the HAC matrix (**figures 14b and 14c).**

The micron-sized calcium carbonate nanostructured crystallites filling the cells of the tissue-like multi-filament wires can be interpreted to have formed due to increased concentration of the impurities originally present in the plant residues when exposed to the flash heating of the spark discharge during the step 1 operation. This pattern strongly resembles the one of mineral particles in ash residues from flash pyrolysis of biomass combustible [18]. Here, the translucent aspect and the composition of the HAC show that the fast rate heating has not induced pyrolysis of the organic carbon but instead its transformation into HAC compounds simultaneously to the growth of carbonate nanocrystallites in the plant cells. This singular

thermal transformation of micron-sized organic compounds immersed in the liquid is viewed to express the profusion of hydrogen issued from the electric decomposition of heptane, which contributed to instantaneously form new molecules by reaction with the activated ions, thus preserving the plant cell structure with their newly formed crystallites. The presence of structural heterogeneities with concentration of heterogeneous impurities observed at nanoscale clearly shows that this subtype of millimeter-sized multi-filament wire is in fact a flattened coalescence of micron-sized residues and not a single plant fragment. Although the visual control with the ultrafast camera does not allow us to finely view the wire morphology during growth, the similar filamentary structure of all the type 2 components confirms their common formation during the step 2 operation. Therefore, the tissue-like multi-filament wires are concluded to have formed during the step 2 by agglomeration of the micron-sized transformed plant residues and of the HAC clusters produced during the step 1 process.

The flat translucent films (subtype 2c) with their particular crumpled paper-sheet morphology share strong resemblance with the tissue-like filamentary wires (subtype 2d) by the abundance of nanostructured microcrystals embedded within the HAC matrix and the evidence of a cell pattern. The lack of a filamentary morphology at microscales and the profusion of finely imbricated nanosized filaments suggest that the step 2 operation has agglomerated step 1 HAC clusters and plant tissues that were originally in the form of a thin film without a distinctive biotic structure. The latter may have been altered by diagenetic alteration during the differentiation of the hydrocarbon precursor as for long established in kerogen petrography [19].

The single and multi- filament wires of the type 2 nanocomposites (subtype 2a & 2b) do not present tissue-like fragment and clearly show continuity from nano- to micro-scales in the chain alignment of the HAC clusters that appear strongly imbricated. A similar diversity of nano- to micron-sized impurities as the ones of the other type 2 nanocomposites is observed

both at the surface of the wires or at the contact between the assembled nano-sized filaments. The continuity of the regular cylindrical morphology all along the wire length in spite of the irregularly distributed micron-sized mineral particles shows that the latter did not constrain the growth process.

In contrast to the subtype 2c and 2d wires, the 2a and 2b cylindrical filamentary ones are thus concluded to have grown during the step 2 operation by a regularly chain agglomeration of the step 1 charged by HAC clusters. Thus, the resulting nanocomposites can be viewed as abiotic filamentary wires although part of the HAC clusters might have originated from plant debris decomposed by the step 1 electric discharge together with the ones issued from the step decomposition of the liquid heptane. The high-resolution SEM or TEM data do not allow at present any distinction between possible difference in size and or composition of the HAC nanoclusters, which would relate to these two sources.

The fact that wires are longer than the inter-electrode gap can be explained by the distribution of the charged HAC clusters when high voltage is applied between the electrodes (**figure 3**). The HAC clusters have thus organized along the field lines to form chains that could have been two or three times longer than the gap distance, *i.e.*, several millimeters. This long continuous growth process implies that the wire remained trapped between the electrodes because the controlled applied voltage prevented any marked increase of the fluid velocity. Thus, the wire growth process is confirmed to have occurred by different forces interacting on the "neutral particle cloud" trapped between the electrodes: gravity, buoyancy, the electrostatic force due to the applied voltage, and convection induced by the fluid motion. The common occurrence of twisted nano-sized filaments, wire folding with formation of filamentary balls or wire assembly wrapping the long multi-filament wire perpendicular to the initial growth direction, reflect slight variations through time of the interacting forces. This assignment is well supported by the visual control with the ultrafast camera that showed how

slight changes of the inter-electrode gap instantaneously modify the overall morphology of the filamentary wire but not its nanostructuration pattern (**figure 3**).

Similarly to the subtype 2c and 2d nanocomposites, the strong cohesion of the subtype 2a and 2b filamentary wires indicates that irreversible agglomeration by HAC cluster polymerization occurred simultaneously to their alignment by the interacting electric forces. As formerly stated, the diverse impurities issued from the step 1 heptane decomposition and electrode erosion might have provided a profusion of the most efficient nanocatalysts required to initiate the polymerization. The restricted quantity of filamentary wires obtained for each experiment with the different sets of electrodes has not allowed yet to test up to what extent the different colours (blue, red, translucent or black) of the filamentary wires would relate to the composition and/or size of the nanoparticles integrated to the HAC clusters from the step 1 operation or to other factors. For similar reasons and in addition to the difficulty of visualizing at high-resolution the 3D-geometry of the HAC nanocluster chains with the associated mineral and metal nanoparticles, the exact role of the latter on the assembly of the nano-sized filaments or on structural defects at nano- to micro-scales of the wires (*e.g.*, twisting, cavities) cannot be further elucidated. In contrast, the common occurrence and diversity of micron-sized mineral and metal particles encountered within the HAC matrix of the subtype 2 filaments and at their surfaces, whereas they were nearly not detected in the type 1 carbon agglomerates on the silica wafer, clearly documents how the maintenance of the electric field during the step 2 operation has led to increase concentrations of impurities in the "charged particulate cloud" trapped in the inter-electrode zone. The presence of nanostructured crystallites, particularly quartz or silicon, with euhedral shape and impinged metal droplets at the crystal surfaces, illustrates how the electric field segregates chemical species which can generate various nanocrystallites showing great diversity and compositional defects at microscale.

4. CONCLUSION AND PERSPECTIVES

The experimentation reported here has allowed us to further refine the forming processes and the controlling factors involved in the synthesis of filamentary nanocomposites from a dielectric liquid under high electric field. At first, our complementary exploration reinforces the critical importance of the initial spark discharges (step 1) for producing hydrogenated amorphous carbon (HAC) from heptane decomposition and associated impurities from electrode erosion. Unexpectedly, the multi-scale investigation performed on the different zones of the experimental setup has revealed that the impurities are jointly issued from the electrodes and from the liquid heptane itself. Even more surprising, solid micro-particles that were originally present in the latter appear to have resisted to the step 1 spark discharge and to have remained trapped in the "charged particulate cloud" formed between the two electrodes. During the second step, the increased inter-electrode gap distance from 100 µm to 1 mm to avoid breakdown was confirmed to create a suite of interacting forces efficient to assemble the HAC nanoclusters in wires by dielectrophoretic transport.

In agreement to previous studies [13, 14], our observation emphasizes the role of dielectrophoresis process to form the chain-like assembly of nanoparticles to the simultaneous separation of compound particle mixtures by size and to co-synthesize nanostructured microcrystals.

In contrast, the refined morphological study of the synthesized products reveals the major role of concurrent polymerization process to produce composite nanostructures of great stability even after removal of the applied electric field. Various metal particles issued from the different source materials are shown to have provided a profusion of catalysts for the irreversible consolidation of the polymerized carbonaceous matrix. The link that we have established between the solid particles originated from the liquid heptane and the

morphological diversity at nano- to micro-scales of the filamentary wires provides an innovative contribution to the knowledge of nanocomposite synthesis triggered by electric field.

Factors explaining how plant micro-particles were not carbonized by the spark discharge in the heptane and got assembled under the coupled action of DEP and polymerization into filamentary nanocomposites resembling biotic tissues requires to be fully elucidated. Also, further research should help us to increase the production of the cylindrical filamentary wires by discharges in liquids in order to determine the relevance of their distinctive properties (color and composition) with respect to the source materials and the discharge conditions.

REFERENCES

[1] Graham WG, Stalder KR (2011) Plasmas in liquids and some of their applications in nanoscience. J Phys D: Appl Phys 44:174037

[2] Ashkarran AA (2011) Metal and metal oxide nanostructures prepared by electrical arc discharge method in liquids. J Clust Sci 22:233–266

[3] Belmonte T, Hamdan A, Kosior F, Noël C, Henrion G (2014) Interaction of discharges with electrode surfaces in dielectric liquids: application to nanoparticle synthesis. J Phys D: Appl Phys 47:224016

[4] Burakov VS, Nevar EA, Nedel'ko MI, Tarasenko NV (2015) Synthesis and modification of molecular nanoparticles in electrical discharge plasma in liquids. Russ J Gen Chem 85:1222–1237

[5] Saito G, Akiyama T (2015) Nanomaterial synthesis using plasma generation in liquid. J Nanomater 2015:123696

[6] Liu S-M, Kobayashi M, Sato S, Kimura K (2005) Synthesis of silicon nanowires and nanoparticles by arc-discharge in water. Chem Commun 37:4690–4692

[7] Sano N, Tamon H (2014) Submerged arc discharge technique to explore novel non-carbon nanotubes: Syntheses of nanotubes from ZnO and $BaTiO_3$. Jap J Appl Phys 53:048002

[8] Sagara T, Kurumi S, Suzuki K (2014) Growth of linear Ni-filled carbon nanotubes by local arc discharge in liquid ethanol. Appl Surf Sci 292:39–43

[9] Yao WT, Yu SH, Zhou Y, Jiang J, Wu QS, Zhang L, Jiang J (2005) Formation of uniform CuO nanorods by spontaneous aggregation: Selective synthesis of CuO, Cu_2O, and Cu nanoparticles by a solid− liquid phase arc discharge process. J Phys Chem B 109 14011–14016

[10] Krishnan S, Haseeb ASMA, Johan MR (2013) Synthesis and growth kinetics of spindly CuO nanocrystals via pulsed wire explosion in liquid medium. J Nanopart Res 15:1410

[11] Xie SY, Ma ZJ, Wang CF, Lin SC, Jiang ZY, Huang RB, Zheng LS (2004) Preparation and self-assembly of copper nanoparticles via discharge of copper rod electrodes in a surfactant solution: a combination of physical and chemical processes. J Solid State Chem 177:3743–3747

[12] Hermanson KD, Lumsdon SO, Williams JP, Kaler EW, Velev OD (2001) Dielectrophoretic assembly of electrically functional microwires from nanoparticle suspensions. Science 294:1082–1086

[13] Velev OD, Gangwal S, Petsev DN (2009) Particle-localized AC and DC manipulation and electrokinetics. Ann Rep C Phys Chem 105:213–246

[14] Lumsdon SO, Kaler EW, Velev OD (2004) Two-dimensional crystallization of microspheres by a coplanar AC electric field. Langmuir 20:2108–2116

[15] Hamdan A, Noël C and Belmonte T (2014) Synthesis of carbon fibres by electrical discharges in heptane. Mater Lett 135:115–118

[16] Hamdan A, Noël C, Ghanbaja J, Migot-Choux S, Belmonte T (2013) Synthesis of platinum embedded in amorphous carbon by micro-gap discharge in heptane. Mater Chem Phys 142:199–206

[17] Witten TA and Sander LM (1983) Diffusion-limited aggregation. Phys Rev B 27:5686–5697

[18] Ludvigsson L, Meuller BO, Messing, ME (2015) Investigations of initial particle stages during spark discharge. J Phys D: Appl Phys 48:314012

[19] Molinder, R., Sandström, L., Wiinikka, H. (2016) Characteristics of particles in pyrolysis oil. Energy Fuels 30(11) 9456–9462

[20] Durand B., Monin JC, Kerogen: Insoluble Organic Matter from Sedimentary Rocks. Chap. 4: Elemental analysis of kerogens (C, H, O, N, S, Fe) (1980), Edition TECHNIP, Ed. by Bernard Durand, Paris.

CAPTIONS

Table 1. Typology and properties of the filamentary nanocomposites**.**

Table 2. Type of nanocomposites and domains of synthesis.

Figure 1: Pictures of the inter-electrode gap. (a) Fluid at rest at $t = T_0$. The electrodes are covered in soot. (b) Discharge event observed at $t = T_0 + 4$ ms. (c) Cloud of carbon nanoparticles aligned along the electric field lines at $t = T_0 + 8$ ms. (d) Same cloud observed at $t = T_0 + 12$ ms.

Figure 2: Time evolution of material formation within the inter-electrode gap area. Distance between the electrodes: 1 mm. Applied voltage: +10 kV. Read vertically from top left to bottom right. First three columns on the left: from 0 to 972 ms. Next four columns: from 1.44 to 4.932 s. At 4.912 s, a new discharge occurs

Figure 3: Wire dynamics in the inter-electrode gap. (a) When the gap size is reduced. (b) When the gap size is increased. Carbon electrodes. Applied Voltage 10 kV.

Figure 4: Main types of nanocomposites viewed under the binocular microscope. (a) Red cylindrical filamentary wire. (b) Translucent multi-filament wire embedding a synthesized quart particle. (c) Brown flat translucent film. (d) Tissue-like multi-filament wire. (e) Translucent crumpled paper-like agglomerate. (f) White mineral-carbonaceous particle.

Figure 5: (a) Type 1 agglomerate on the aluminium anode showing abundant aluminium spherules embedded in the black carbonaceous matrix (BSE-SEM). (b) Detailed view showing the abundance of metal and mineral inclusions (bright grains) in the black carbonaceous matrix (BSE-SEM). (c) Type 1 agglomerate on the silicon wafer for the aluminium electrode experiment showing the black carbonaceous matrix with aluminium spherules and the metal particles dominantly formed of Cu-Ni (bright grains)- BSE-SEM. (d) Type 3 metal particle on the copper cathode showing intermixing of bismuth and cadmium (BSE-SEM).

Figure 6: Examples of type 2 carbonaceous-metal filamentary wires. (a) Subtype 2a cylindrical filamentary wire made of densely packed twisted nano-sized filaments with metal particles (bright grains). (b) Subtype 2b multi-filament wire made of an assembly of strands of smaller diameters. (c) Subtype 2d filamentary wire with plant structure. (d) Crumpled paper-like flaky agglomerate. BSE-SEM.

Figure 7: Micropattern of mineral and metal particles associated to type 2 carbonaceous-metal filamentary wires. (a) Subtype 2b twisted multifilament wire. (b) Detailed view showing a Fe-Cr-Ni nanostructured rod, an angular quartz and needle-shape alumino-silicate. (c) Subtype 2c flat translucent film. (d) Detailed view showing abundant particles made of barium sulphate, calcium carbonate and calcium chloride. BSE-SEM.

Figure 8: Micro-pattern of type 2 filamentary wires. (a) Subtype 2a twisted wire showing a nanostructural pattern of the folded matrix. BSE-SEM. (b) Subtype 2b multifilament wire (cf. figure 6b) showing the very fine nanostructural pattern of elementary filament. SE-SEM. (c) Dense imbrication of nanostructured filament for a subtype 2b multifilament wire. SE-SEM. (d) Plant cell with carbonate inclusion (in bright) in a subtype 2d wire (cf. figure 6c). BSE-SEM.

Figure 9: Nano-pattern of type 2 filamentary wires. (a) Detailed view of a crumpled paper-like flaky agglomerate (cf. figure 6d). SE-SEM. (b) High-resolution view showing the fine folding of the nanostructured film and the presence of coarse nanoparticles. SE-SEM. (c) Detailed view of a subtype 2b multi-filament wire (cf. figure 6b). SE-SEM. (d) High-resolution view showing the euhedral calcium carbonate nanocrystallites embedded in the nanostructured carbonaceous matrix. SE-SEM.

Figure 10: (a) SEM image of a single strand wire. Inserts are higher resolution images showing the agglomeration of nanoparticles at the origin of the wire structure. (b) Low-resolution TEM image showing a wire made between nickel electrodes. (c) High-resolution

TEM image showing the presence of Ni nanoparticles (dark dots) in the network of HAC nanoparticles.

Figure 11: Type 3 mineral particles. (a) Synthesized quartz (cf. figure 4b). (b) Detailed view showing Fe-Cr-Ni metal coating on the edges and the irregular surface. BSE-SEM. (c) Composite mineral aggregate made of calcium carbonate and alumino-silicate (cf. figure 4f) cemented by carbonaceous film. BSE-SEM. (d) Angular flake of silicon. (e) Detailed view showing the nanostructural pattern. SE-BSE. (f) Detailed view of the parallel nanostructures with Fe-Cr-Ni particles. BSE-SEM.

Figure12: FTIR spectra of wires elaborated with different electrode materials (C, W, Al, Ni, and Cu).

Figure 13: Comparison of multi-strand wire tips (a) after synthesis by discharges in liquids (b) after dielectrophoresis. Reproduced with permission from Science. After [12].

Figure 14: (a) Example of wire synthesized using graphite electrodes. (b) Low-resolution and (c) high-resolution TEM images showing the HAC sheet.

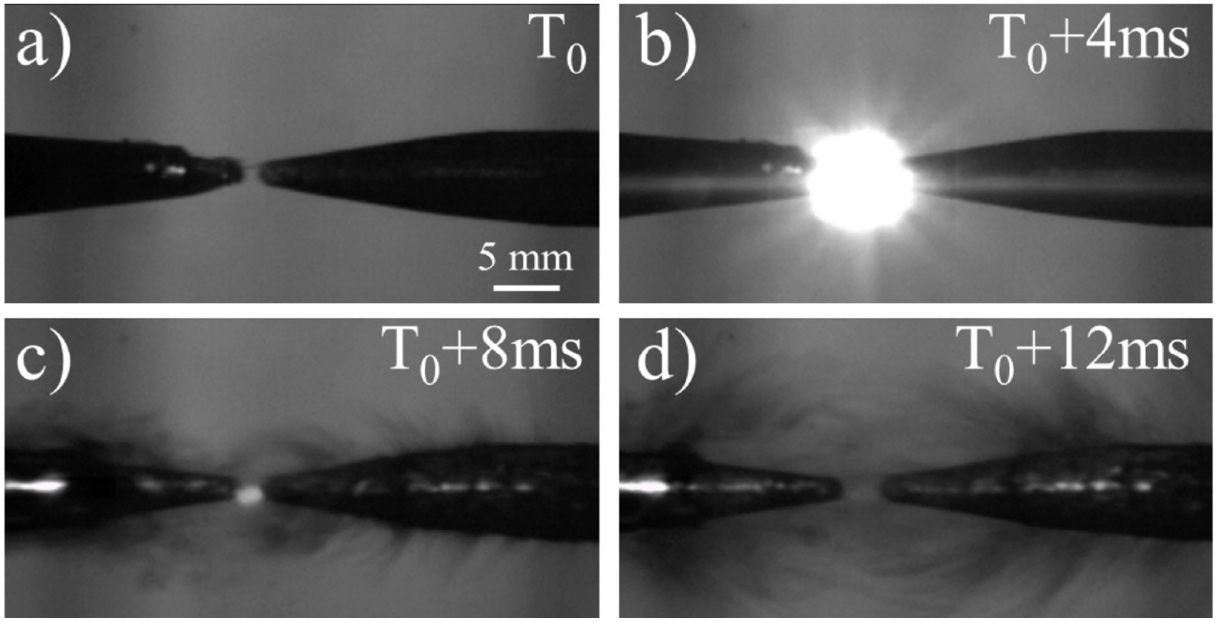

Figure 1: Pictures of the inter-electrode gap. (a) Fluid at rest at $t = T_0$. The electrodes are covered in soot. (b) Discharge event observed at $t = T_0 + 4$ ms. (c) Cloud of carbon nanoparticles aligned along the electric field lines at $t = T_0 + 8$ ms. (d) Same cloud observed at $t = T_0 + 12$ ms.

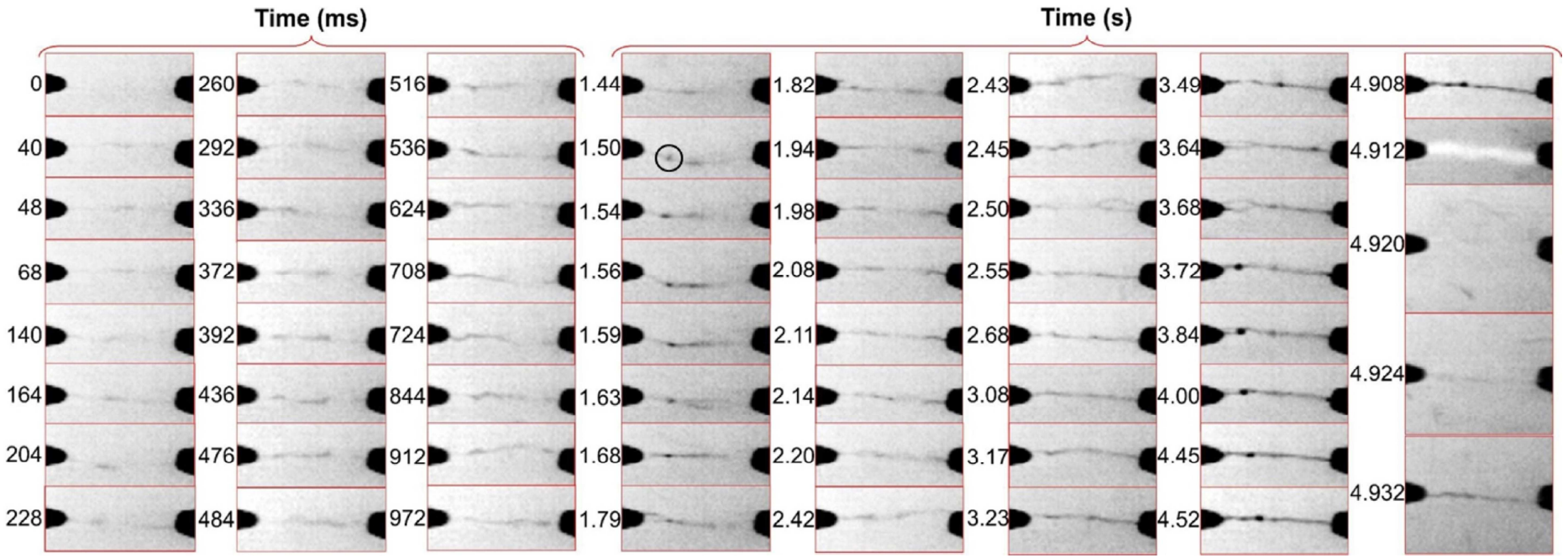

Figure 2: Time evolution of material formation within the inter-electrode gap area. Distance between the electrodes: 1 mm. Applied voltage: +10 kV. Read vertically from top left to bottom right. First three columns on the left: from 0 to 972 ms. Next four columns: from 1.44 to 4.932 s. At 4.912 s, a new discharge occurs.

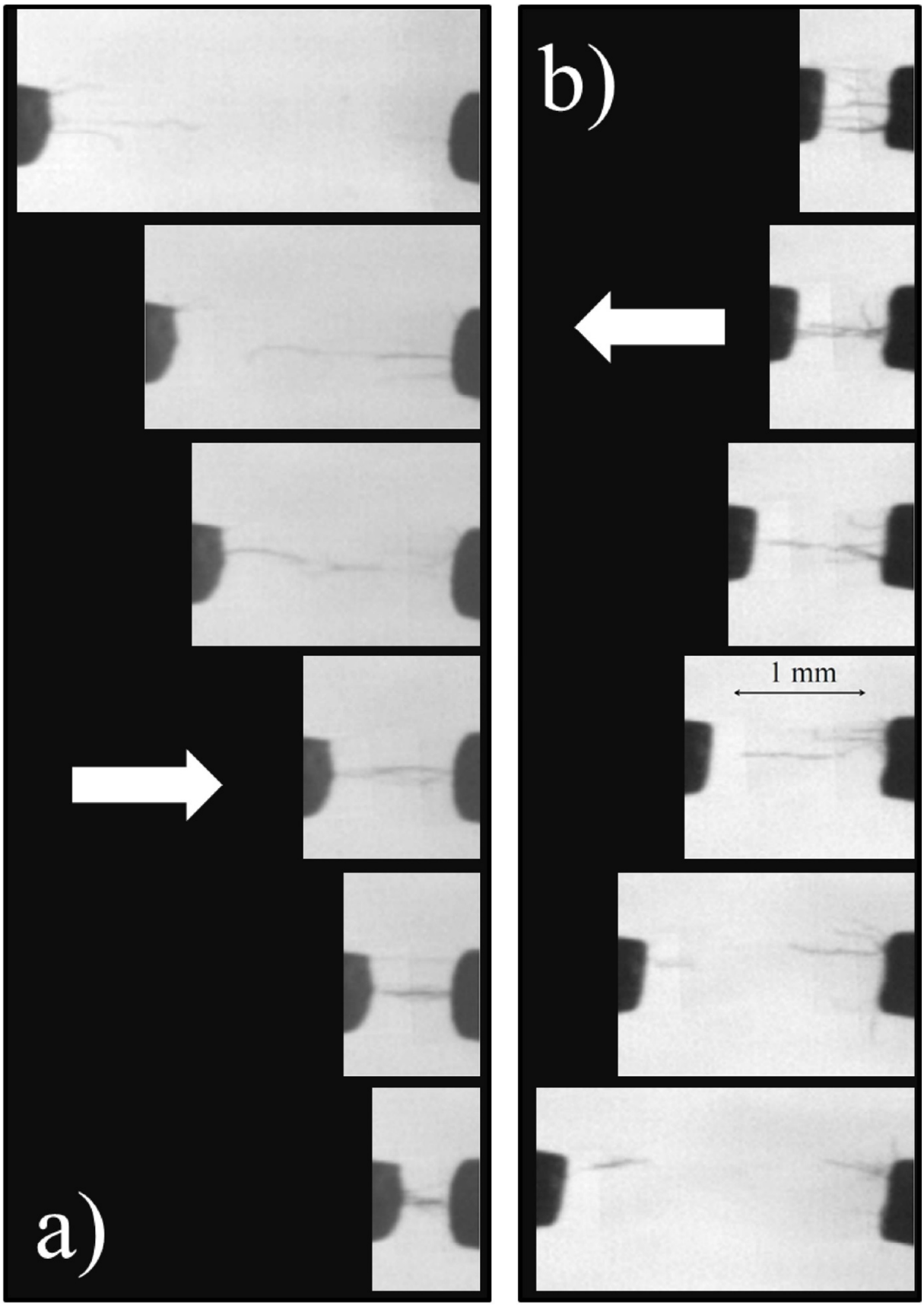

Figure 3: Wire dynamics in the inter-electrode gap. (a) When the gap size is reduced. (b) When the gap size is increased. Carbon electrodes. Applied Voltage 10 kV.

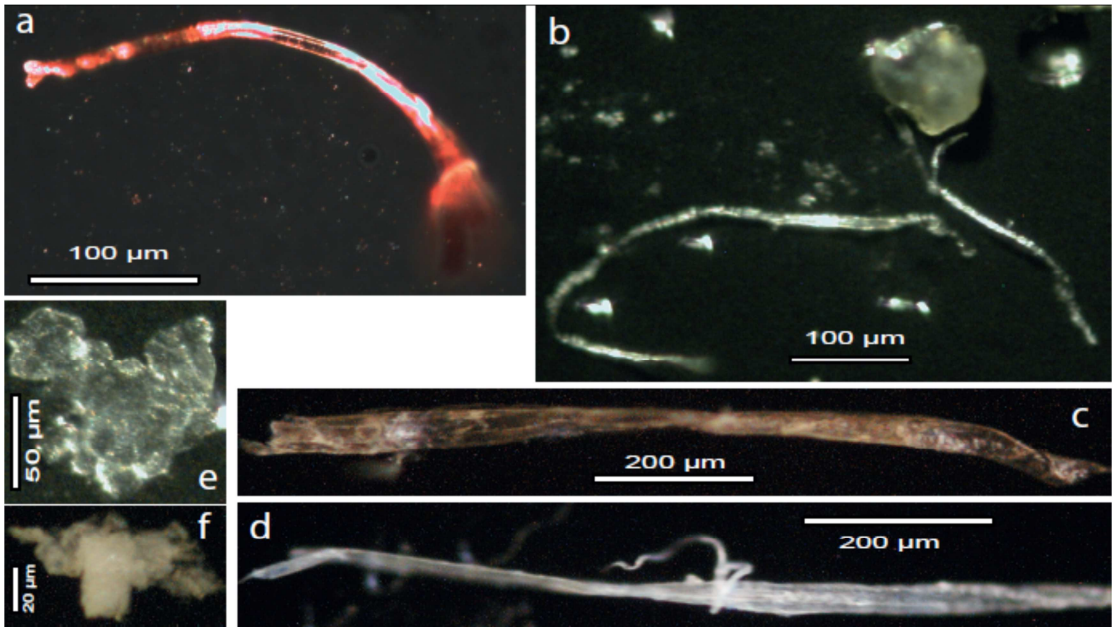

Figure 4: Main types of nanocomposites viewed under the binocular microscope. (a) Red cylindrical filamentary wire. (b) Translucent multi-filament wire embedding a synthesized quart particle. (c) Brown flat translucent film. (d) Tissue-like multi-filament wire. (e) Translucent crumpled paper-like agglomerate. (f) White mineral-carbonaceous particle.

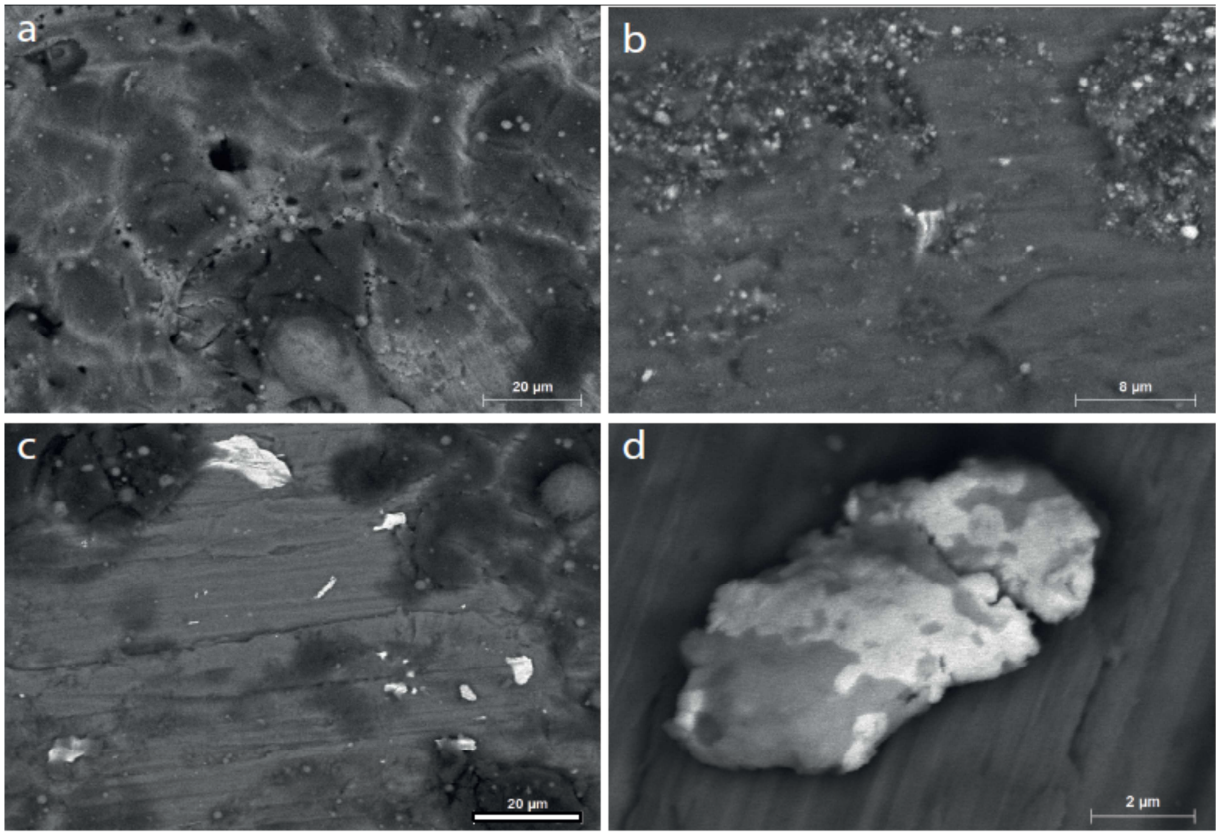

Figure 5: (a) Type 1 agglomerate on the aluminium anode showing abundant aluminium spherules embedded in the black carbonaceous matrix (BSE-SEM). (b) Detailed view showing the abundance of metal and mineral inclusions (bright grains) in the black carbonaceous matrix (BSE-SEM). (c) Type 1 agglomerate on the silicon wafer for the aluminium electrode experiment showing the black carbonaceous matrix with aluminium spherules and the metal particles dominantly formed of Cu-Ni (bright grains)- BSE-SEM. (d) Type 3 metal particle on the copper cathode showing intermixing of bismuth and cadmium (BSE-SEM).

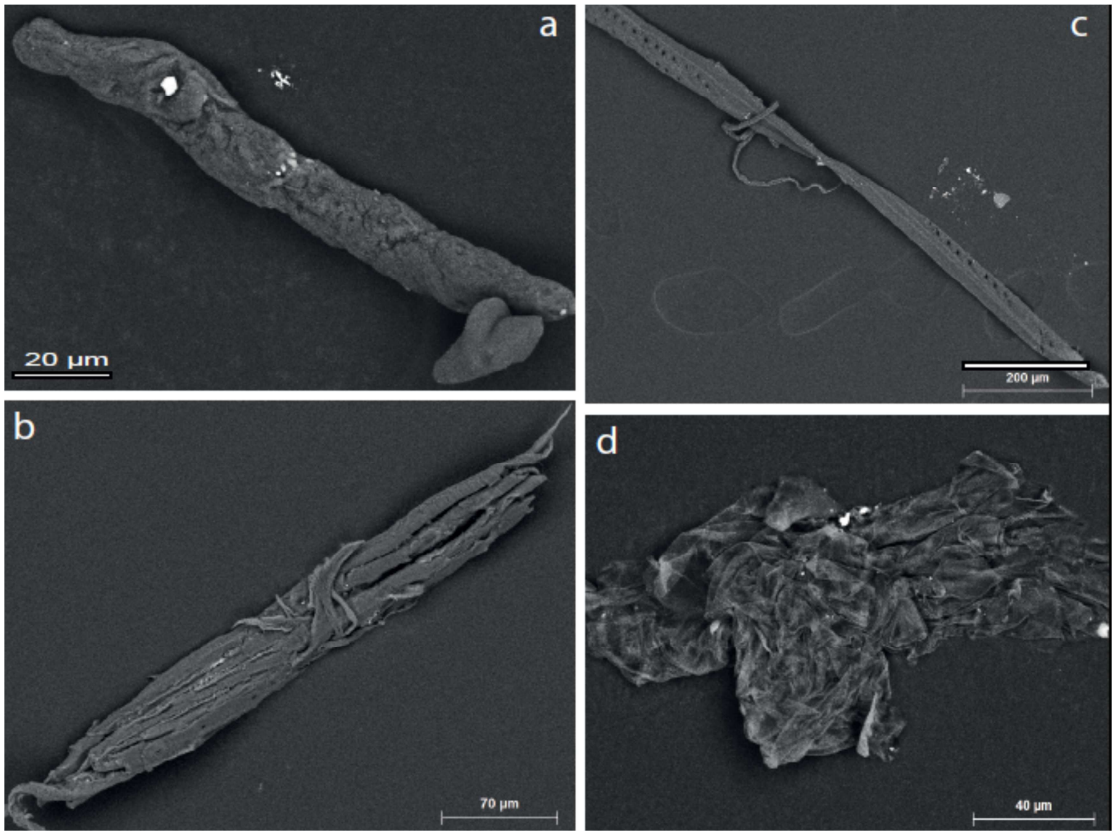

Figure 6: Examples of type 2 carbonaceous-metal filamentary wires. (a) Subtype 2a cylindrical filamentary wire made of densely packed twisted nano-sized filaments with metal particles (bright grains). (b) Subtype 2b multi-filament wire made of an assembly of strands of smaller diameters. (c) Subtype 2d filamentary wire with plant structure. (d) Crumpled paper-like flaky agglomerate. BSE-SEM.

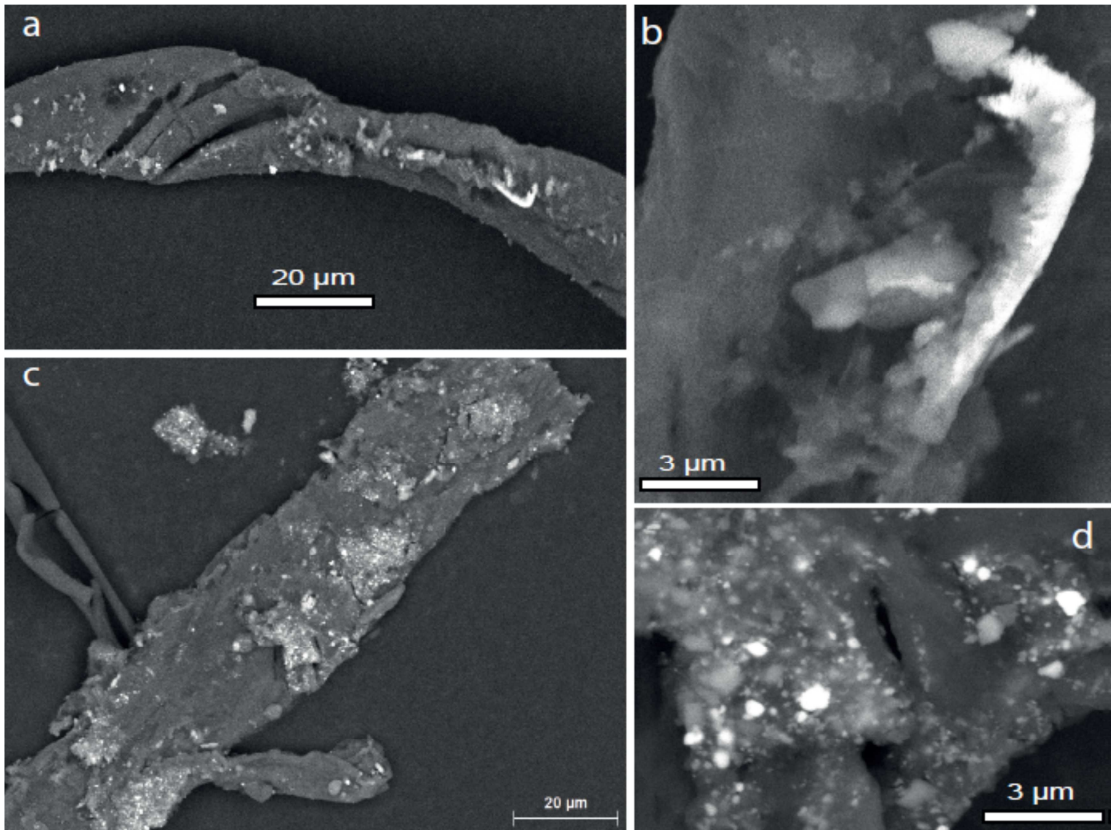

Figure 7: Micropattern of mineral and metal particles associated to type 2 carbonaceous-metal filamentary wires. (a) Subtype 2b twisted multifilament wire. (b) Detailed view showing a Fe-Cr-Ni nanostructured rod, an angular quartz and needle-shape alumino-silicate. (c) Subtype 2c flat translucent film. (d) Detailed view showing abundant particles made of barium sulphate, calcium carbonate and calcium chloride. BSE-SEM.

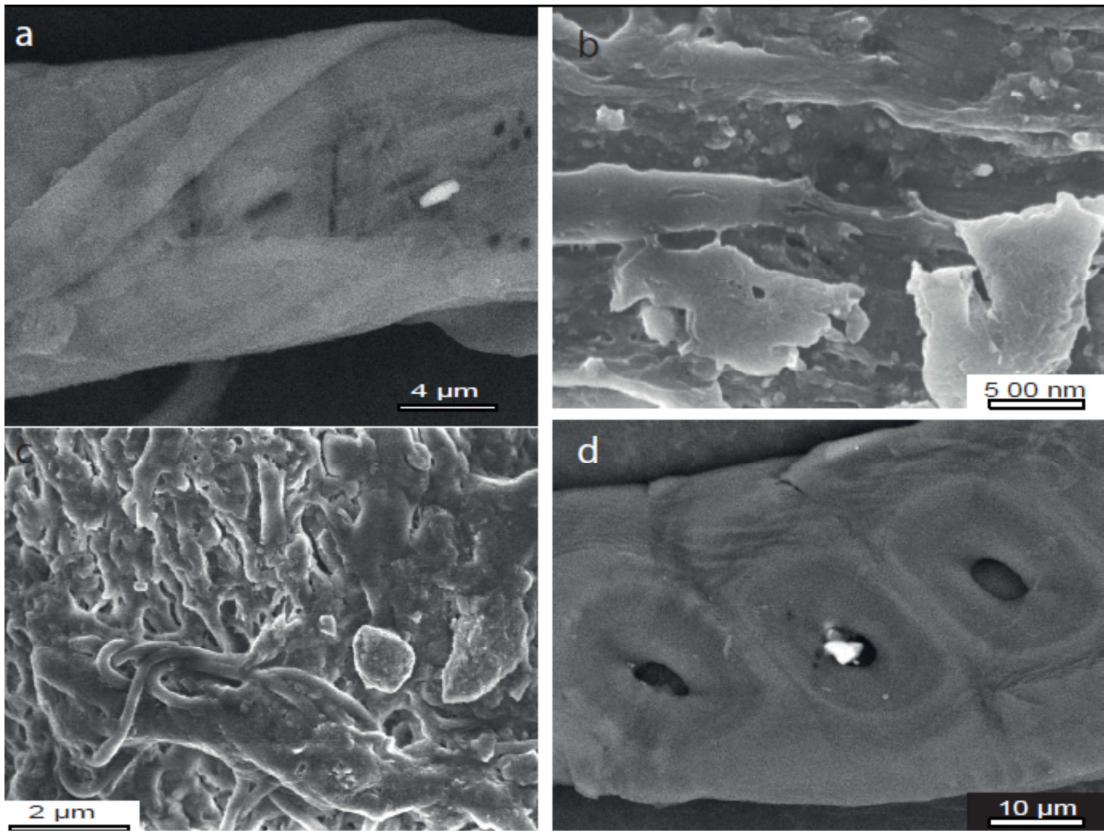

Figure 8: Micro-pattern of type 2 filamentary wires. (a) Subtype 2a twisted wire showing a nanostructural pattern of the folded matrix. BSE-SEM. (b) Subtype 2b multifilament wire (cf. figure 6b) showing the very fine nanostructural pattern of elementary filament. SE-SEM. (c) Dense imbrication of nanostructured filament for a subtype 2b multifilament wire. SE-SEM. (d) Plant cell with carbonate inclusion (in bright) in a subtype 2d wire (cf. figure 6c). BSE-SEM.

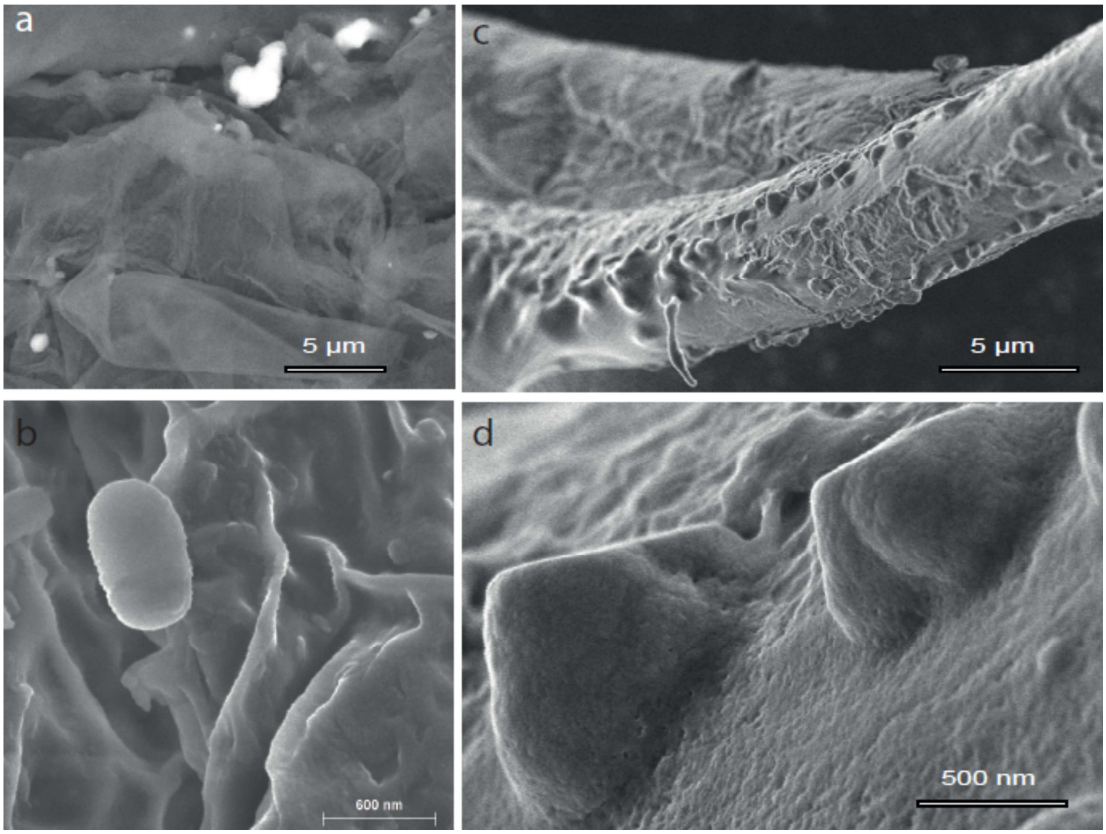

Figure 9: Nano-pattern of type 2 filamentary wires. (a) Detailed view of a crumpled paper-like flaky agglomerate (cf. figure 6d). SE-SEM. (b) High-resolution view showing the fine folding of the nanostructured film and the presence of coarse nanoparticles. SE-SEM. (c) Detailed view of a subtype 2b multi-filament wire (cf. figure 6b). SE-SEM. (d) High-resolution view showing the euhedral calcium carbonate nanocrystallites embedded in the nanostructured carbonaceous matrix. SE-SEM.

.

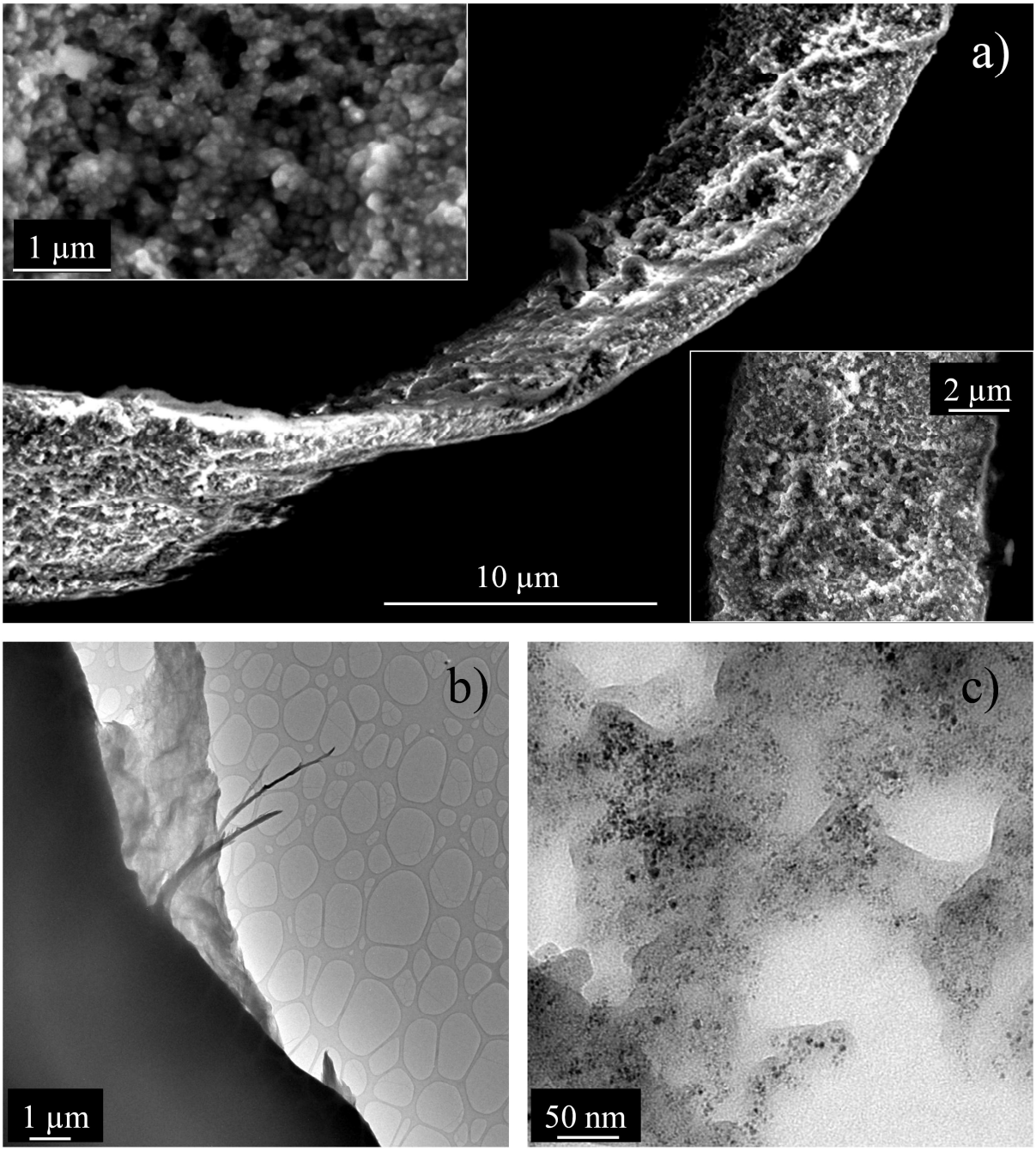

Figure 10: (a) SEM image of a single strand wire. Inserts are higher resolution images showing the agglomeration of nanoparticles at the origin of the wire structure. (b) Low-resolution TEM image showing a wire made between nickel electrodes. (c) High-resolution TEM image showing the presence of Ni nanoparticles (dark dots) in the network of HAC nanoparticles.

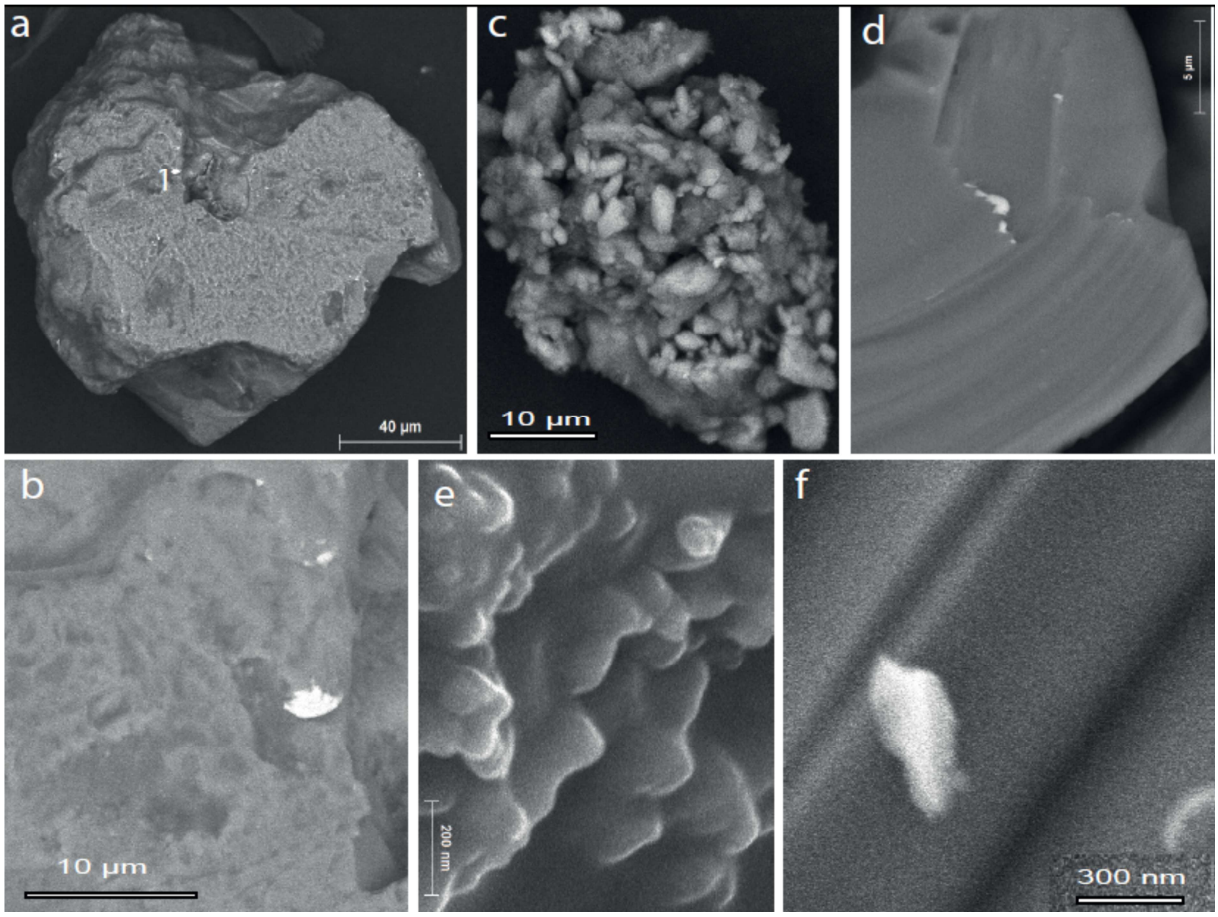

Figure 11: Type 3 mineral particles. (a) Synthesized quartz (cf. figure 4b). (b) Detailed view showing Fe-Cr-Ni metal coating on the edges and the irregular surface. BSE-SEM. (c) Composite mineral aggregate made of calcium carbonate and alumino-silicate (cf. figure 4f) cemented by carbonaceous film. BSE-SEM. (d) Angular flake of silicon. (e) Detailed view showing the nanostructural pattern. SE-BSE. (f) Detailed view of the parallel nanostructures with Fe-Cr-Ni particles. BSE-SEM.

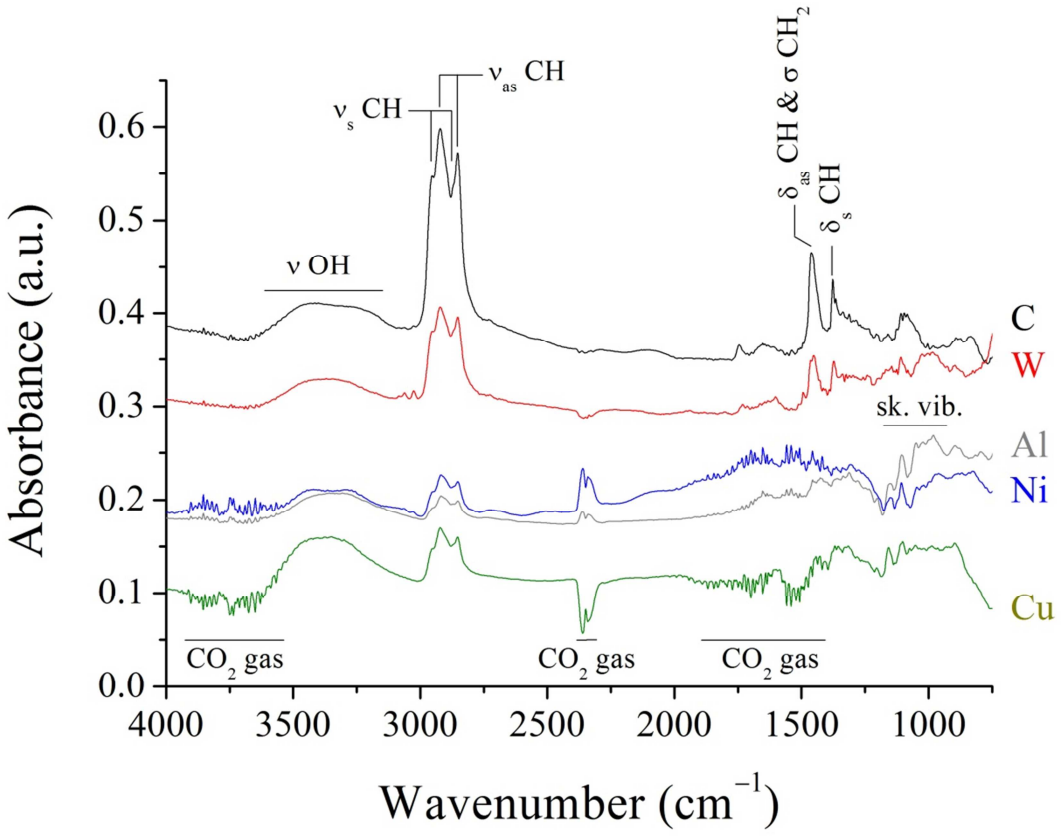

Figure 12: FTIR spectra of wires elaborated with different electrode materials (C, W, Al, Ni, and Cu).

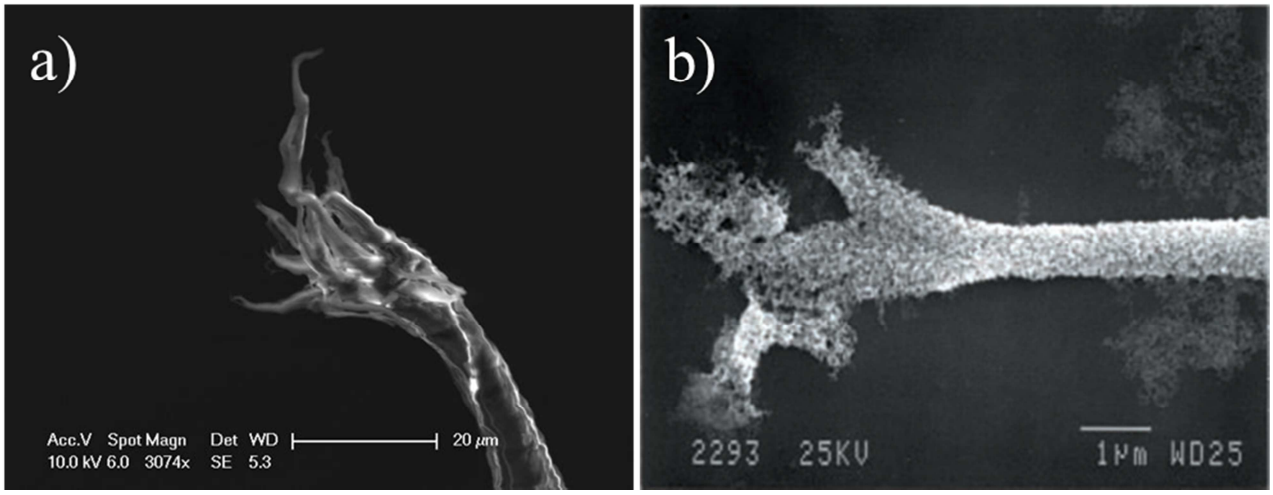

Figure 13: Comparison of multi-strand wire tips (a) after synthesis by discharges in liquids (b) after dielectrophoresis. Reproduced with permission from Science. After [12].

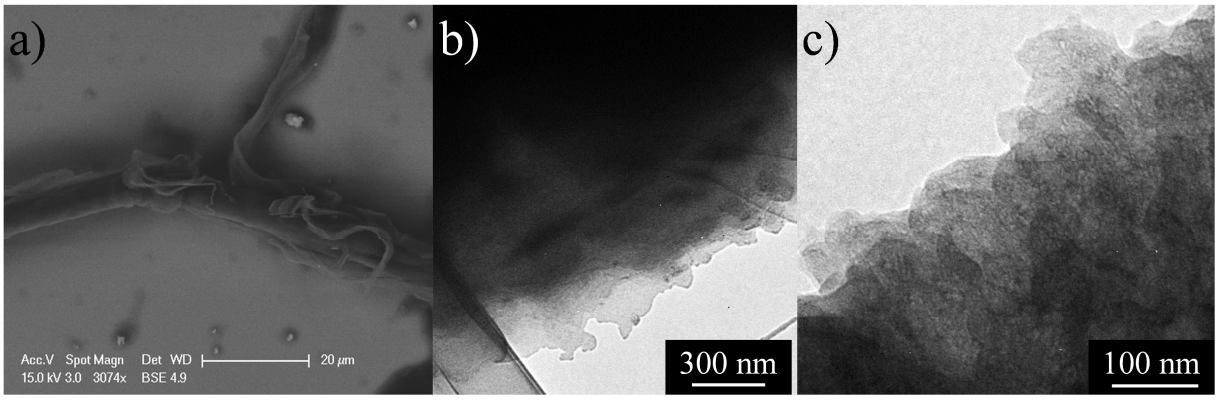

Figure 14: (a) Example of wire synthesized using graphite electrodes. (b) Low-resolution and (c) high-resolution TEM images showing the HAC sheet.

Table 1. Typology and properties of the filamentary nanocomposites**.**

Type	Aspect	Assemblage	Inclusions
a. Single filamentary wires	Long, dense Blue, red, translucent,black	densely packed, twisted nano-sized filaments	$CaCO_3$/C (FeO/Fe-Cr (red) C O Al Si C O Al S SiO_2 (Cu) Cu spherules Al Si K $CaSO_4$ MgSiCa (Cu) $FeMgCO_3$ (Cu) Fe Ca (Cu) Fe Ca (Cu) MgAlCaFe/SiO_2 /SCa
b. Multi- filament wires	Long, porous, twisted bundles	Micron-sized filaments; nanoparticle chain alignment and micro-particle inclusions	$FeCr/CaCO_3$ Carbonaceous matrix/Al S/SiO_2/ Al Si K $CaSO_4$/Cu spherules Carbonaceous/Ca C/ FeCrNi Fe Bright grain/ Ca KCl S/Ag Au Pd In $FeCr/CaCO_3$ Carbonaceous matrix/Al S/SiO_2/ Al Si K $CaSO_4$/Cu spherules Carbonaceous/Ca C/ FeCrNi Fe Bright grain/ Ca KCl S/Ag Au Pd In
c. Flat translucent films	Short, sharp edges, crumpled sheet	Euhedral coarse NP; not organized (1/2 µm) Dense packing of nano to micron-sized particles Microcrystals with euhedral shape formed of network of nanoparticles Nanostructured; dense packing of nanoparticles; scattered micron-sized metal particles	Al Si K $BaSO_4$ AlSiFe AlSiTi Al matrix/FeCr Al matrix/Si Al matrix/CaC, Cl, KCl C matrix /Ca Al matrix/ FeCr Al matrix/ Fe Al matrix/ CaC C matrix/ KCl/C Ca/C S Cl C/AlMgSiFe/FeCrNi Al/ Ca S/Zn & sulfate/Zn pure/ Ca S/Cl Ag/Ca &C/im2
d. Tissue-like multi-filament wires	Short to long, sharp edges, twisted, cell structure	Not nanostructured. Micron-sized nanostructured inclusions;	Al/Fe Carbonaceous matrix/ $CaCO_3$/CaC Carbonaceous matrix/ $CaCO_3$/FeCr/Si Carbonaceous matrix/ Ca MgAlCaFe/SiO_2/SCa WAu K Cl $CaCO_2$ SO_4Sr FeCrNi

Table 2. Type of nanocomposites and domains of synthesis.

Type/ Domains	**Agglomerates**	**Filamentary wires**	**Metal particles**	**Mineral particles**
Cathode (-/D1a)			+++	
Anode (b/D1b)	+++			+++
Inter-electrode domain		+++++	++	+++
Arc-affected domain	++++	(t)	++	(t)

+ : abundance estimation
t : traces